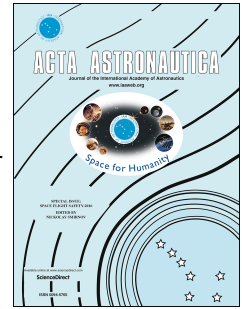


# Accepted Manuscript

Numerical study on the aerothermodynamics of different heatshield configurations for Mars entry capsules

Kang Zhong, Chao Yan, Shu-sheng Chen, Xiao-yong Wang, Sheng-jun Ju



PII: S0094-5765(18)31711-9

DOI: <https://doi.org/10.1016/j.actaastro.2018.12.025>

Reference: AA 7247

To appear in: *Acta Astronautica*

Received Date: 22 October 2018

Revised Date: 13 December 2018

Accepted Date: 20 December 2018

Please cite this article as: K. Zhong, C. Yan, S.-s. Chen, X.-y. Wang, S.-j. Ju, Numerical study on the aerothermodynamics of different heatshield configurations for Mars entry capsules, *Acta Astronautica* (2019), doi: <https://doi.org/10.1016/j.actaastro.2018.12.025>.

This is a PDF file of an unedited manuscript that has been accepted for publication. As a service to our customers we are providing this early version of the manuscript. The manuscript will undergo copyediting, typesetting, and review of the resulting proof before it is published in its final form. Please note that during the production process errors may be discovered which could affect the content, and all legal disclaimers that apply to the journal pertain.

# Numerical study on the aerothermodynamics of different heatshield configurations for Mars entry capsules

Kang Zhong <sup>a</sup>, Chao Yan <sup>a,\*</sup>, Shu-sheng Chen <sup>a</sup>, Xiao-yong Wang <sup>b</sup>, Sheng-jun Ju <sup>a</sup>

<sup>a</sup> National Key Laboratory of Computational Fluid Dynamics, Beihang University, Beijing 100191, China

<sup>b</sup> Institute of Mechanics, Chinese Academy of Sciences, Beijing 100190, China

## Abstract

Aeroheating predictions play an important role in the heatshield design of Mars entry capsule. This paper numerically investigates the effects of sphere-cone angle on the aerothermodynamic performances of heatshield configurations. Three-dimensional Navier-Stokes equations with chemical non-equilibrium models are employed to simulate the flowfield around the capsule. The laminar and turbulent heating rates of different heatshield configurations are compared and analyzed in detail. A novel correlation for turbulent heating augmentation in terms of laminar momentum thickness Reynolds number is developed to provide a guidance for engineering design and application. The proposed correlation can be more accurate and applicable due to its consideration of the sphere-cone angle effects. Finally, the laminar and turbulent maximum heat flux and total heat load along the flight trajectory are investigated for all the configurations. The numerical study is expected to illustrate the aeroheating characteristics of different heatshield configurations and provide an insight into the rational configuration design for future Mars entry capsules.

## Keywords:

Aeroheating; Heatshield configuration; Sphere-cone angle; Mars; Turbulent.

## Nomenclature

$C_{f,r}$	=	parameter of chemical reaction $r$
$D_s$	=	diffusion coefficient of species $s$
$D_{L,s}$	=	laminar diffusion coefficient of species $s$
$E$	=	total energy
$E_{f,r}$	=	parameter of chemical reaction $r$
$H$	=	total enthalpy
$h_s$	=	enthalpy per unit mass of species $s$
$k$	=	turbulent kinetic energy
$k_{f,r}$	=	forward rate coefficient of chemical reaction $r$
$k_{b,r}$	=	backward rate coefficient of chemical reaction $r$
$Ma$	=	Mach number
$M_s$	=	molecular weight of species $s$
$n_{f,r}$	=	parameter of chemical reaction $r$
$n_s$	=	total number of species
$p$	=	pressure
$P_k$	=	production terms of the turbulent kinetic energy
$P_\omega$	=	production terms of the specific dissipation rate of turbulence
$Pr$	=	laminar Prandtl number
$Prt$	=	turbulent Prandtl number
$q_w$	=	surface heat flux

$\bar{R}$	=	universal gas constant
$Re$	=	Reynolds number
$Re_c$	=	cell Reynolds number
$Re_\theta$	=	laminar momentum thickness Reynolds number
$Sc$	=	laminar Schmidt number
$Sct$	=	turbulent Schmidt number
$T$	=	temperature
$T_d$	=	control temperature
$u_j$	=	$j^{\text{th}}$ velocity component
$Y_s$	=	mass fraction of species $s$
$\alpha$	=	angle of attack
$\alpha_c$	=	sphere-cone angle
$\delta_{ij}$	=	Kronecker delta function
$\varepsilon$	=	surface emissivity
$\eta$	=	thermal conductivity of the mixture
$\kappa$	=	total thermal conductivity
$\mu$	=	total viscosity
$\mu_L$	=	laminar viscosity
$\mu_T$	=	turbulent viscosity
$\rho_s$	=	species density
$\rho$	=	density
$\theta$	=	momentum thickness
$\tau_{ij}$	=	viscous stress tensor
$\phi$	=	turbulent heating augmentation factor
$\omega$	=	specific dissipation rate of turbulence
$\omega_s$	=	mass rate of production of species $s$
$\Omega$	=	magnitude of vorticity

### Subscript

$e$	=	boundary-layer edge
$r$	=	chemical reaction
$s$	=	species
$\infty$	=	freestream

## 1. Introduction

Driven by researches for extraterrestrial life and human exploration missions, Mars has been the most frequently visited planet in the solar system [1-3]. During the hypersonic entry period, the heatshield encounters a severe aerothermodynamic environment characterized by strong shock waves and high temperature, which challenges the thermal protection system (TPS) greatly. Thus, it becomes extremely important to predict the aeroheating accurately and design the suitable heatshield configuration in Mars entry missions.

In previous flights to Mars, the typical configuration of Mars capsules is usually a  $70^\circ$  sphere-cone forebody with a conic or biconic aftbody, such as the Viking [4], Pathfinder [5], Mars Exploration Rover [6] and Phoenix [7]. The latest capsule, Mars Science Laboratory (MSL), which entered the Mars atmosphere successfully in 2012, also

inherited this configuration [8]. However, given its much larger size and weight, MSL experienced much more aggressive atmospheric entry than any of the previous missions [9]. Moreover, because of its large diameter and flying at high angles of attack, forebody boundary-layer transition would occur prior to the peak heat flux time along the flight trajectory [10]. The heating loads acting on the MSL are further exacerbated by the complex turbulent flows.

During the past few years, various significant researches have been performed on MSL's aeroheating predictions [8-16]. Edquist and Wright et al. [9] simulated the hypersonic flowfield around the MSL capsule at the peak heating time using LAURA and DPLR. The numerical results showed that both codes predicted similar turbulent heat flux on the heatshield. In addition, the turbulent heating rates calculated with two different turbulence models, including Baldwin-Lomax model and SST model, were observed to be in reasonable accordance in their studies. Wang et al. [3] investigated the laminar and turbulent aeroheating performances of the MSL capsule with two distinct gas models, namely chemical non-equilibrium model and perfect gas model with specified effective specific heat ratio. Their studies revealed that laminar aeroheating calculated by the two gas models was nearly the same, whereas the turbulent heating rates predicted by chemical non-equilibrium model were much higher than perfect gas model at most areas of the heatshield.

On the other hand, the effects of geometric parameters on aeroheating performances of the MSL heatshield have also attracted considerable attentions in recent years. Neville et al. [17] performed a shape optimization on the heatshield to improve the performance of MSL. Maximizing the drag coefficient and minimizing the peak heat flux were the two objectives in their studies. Brown [18] numerically compared the aerodynamic and aerothermodynamic performances of 70° sphere-cone and ellipsoidal heatshield. He found that compared with 70° sphere-cone, the peak heat flux of ellipsoidal heatshield was reduced by up to 50%. Ju et al. [19] conducted a sensitivity analysis on geometric parameters of the MSL capsule. Three parameters, including the sphere-cone angle, the nose radius and the shoulder radius were considered. Numerical results indicated that for both laminar and turbulent predictions, the sphere-cone angle was the top contributor to the uncertainty of maximum heat flux, and thus they suggested the sphere-cone angle should be firstly deliberated in thermal protection system design. In addition, Hollis et al. [10, 16] carried out transition and aerothermodynamics analysis on the scaled MSL models with different sphere-cone angles in hypersonic wind tunnels. Results showed that the changes of sphere-cone angle induced remarkable differences on the transition onset location and heat flux distributions on the surface.

The above literature survey demonstrates that the sphere-cone angle of heatshield has significant effects on aeroheating performances of the MSL capsule. However, mechanistic and meticulous work on the effects of sphere-cone angle remains relatively insufficient, and several important problems still need further investigations. Firstly, although laminar and turbulent heating predictions of the MSL capsule have been carried out extensively, the relationship between the sphere-cone angle and the aerothermodynamics needs to be further revealed to point out the direction for future design of the Mars entry capsule, especially in the reduction of heating rates acting on the heatshield. Secondly, previous turbulent heating augmentation (turbulent heat flux above laminar) and transition onset correlations, which can be employed as engineering-level design and analysis tools, were fitted by hypersonic wind-tunnel data of scaled 70° sphere-cone models [14, 20]. Unfortunately, no ground-based experiments can fully reproduce the high-speed and high-temperature Martian flow occurring at real flight conditions [21]. Besides, the effects of sphere-cone angle were not included in these correlations. Thus, a novel correlation with consideration of sphere-cone angle effects should be explored to provide a better guidance. Thirdly, since the maximum heat flux and total heat load play an important role in the design of thermal protection system, detailed analysis on these two parameters for different heatshield configurations should be carried out carefully.

In this study, hypersonic flows over the MSL heatshields with sphere-cone angles of 60°, 70° and 80° are numerically investigated by solving three-dimensional Navier-Stocks equations with chemical non-equilibrium models.

Firstly, the flowfield and surface heat flux for different heatshields are analyzed and compared in detail. Then, a novel correlation for turbulent heating augmentation in terms of laminar momentum thickness Reynolds number is developed and verified. Finally, the maximum heat flux and total head load along the flight trajectory for different configurations are investigated. Our numerical study is expected to illustrate the aeroheating characteristics of different heatshield configurations, and meantime provide an insight into the rational configuration design for future Mars entry capsules.

## 2. Numerical methods

Numerical simulations in the present study are performed by an in-house code developed by the authors [3, 22]. The reliability and accuracy of the code have been verified by a series of numerical experiments [3, 22]. Three-dimensional Navier-Stokes equations with chemical non-equilibrium processes are resolved by finite volume method on multi-block structured grids. The main algorithms of the code are presented as follows.

### 2.1 Governing equations

Consider three-dimensional Navier-Stokes equations with chemical non-equilibrium processes [23, 24]

$$\frac{\partial \rho_s}{\partial t} + \frac{\partial \rho_s u_j}{\partial x_j} = \frac{\partial}{\partial x_j} \left( \rho D_s \frac{\partial Y_s}{\partial x_j} \right) + \omega_s \quad (1)$$

$$\frac{\partial \rho u_i}{\partial t} + \frac{\partial \rho u_i u_j}{\partial x_j} = - \frac{\partial p}{\partial x_i} + \frac{\partial \tau_{ij}}{\partial x_j} \quad (2)$$

$$\frac{\partial \rho E}{\partial t} + \frac{\partial \rho H u_j}{\partial x_j} = \frac{\partial}{\partial x_j} \left( \eta \frac{\partial T}{\partial x_j} \right) + \frac{\partial}{\partial x_j} \left( \rho \sum_{s=1}^{ns} h_s D_s \frac{\partial Y_s}{\partial x_j} \right) + \frac{\partial \tau_{ij} u_i}{\partial x_j} \quad (3)$$

where  $\rho_s$  is the density of species  $s$  for  $s=1, \dots, ns$ ,  $\rho$  is the total density of all species,  $Y_s = \rho_s / \rho$  is the mass fraction of species  $s$ ,  $D_s$  is diffusion coefficient of species  $s$ ,  $\omega_s$  is the mass production rate of species  $s$  due to the chemical reactions,  $u_j$  is the  $j^{\text{th}}$  velocity component, and  $ns$  is the total number of all species.  $E$  is the total energy per unit mass of mixture,  $H$  is the total enthalpy per unit mass of mixture,  $T$  is the translational-rotational temperature,  $h_s$  is the enthalpy per unit mass of species  $s$ , and  $\eta$  is the thermal conductivity of the mixture.

The terms of pressure  $p$  and viscous stress tensor  $\tau_{ij}$  are calculated by [23, 24]

$$p = \bar{R} T \sum_{s=1}^{ns} \frac{\rho_s}{M_s} \quad (4)$$

$$\tau_{ij} = \mu \left( \frac{\partial u_i}{\partial x_j} + \frac{\partial u_j}{\partial x_i} \right) - \frac{2}{3} \mu \frac{\partial u_k}{\partial x_k} \delta_{ij} \quad (5)$$

where  $\bar{R}$  is the universal gas constant,  $M_s$  is the molecular weight of species  $s$ ,  $\mu$  is the total viscosity of the mixing species, and  $\delta_{ij}$  is the Kronecker delta function.

Because of the short relaxation time of dominant species in the Martian atmosphere  $\text{CO}_2$ , the level of thermal non-equilibrium in the flowfield is minor [1, 3]. Thus, one temperature model is employed and the vibrational-electronic energy conservation is not included in the current study.

The heat flux  $q_w$  has three contributing components, including the thermal conduction, the diffusion and the radiation. The radiation heat flux is minimal and can be neglected in the current trajectory [9], and therefore, the heat flux  $q_w$  is given by [23, 24]

$$q_w = \eta \frac{\partial T}{\partial n} + \rho \sum_{s=1}^{ns} D_s h_s \frac{\partial Y_s}{\partial n} \quad (6)$$

in which, the subscript  $n$  denotes the normal derivative at the solid surface.

## 2.2 Turbulence model

Menter's shear stress transport (SST) turbulence model is implemented in the current study [25]. The SST model merges the original model in the inner region of boundary layer and the standard model in the outer region and free shear flows [25, 26], and has been shown by Brown [27] to provide accurate simulations of a variety of supersonic and hypersonic flowfields. In particular, the SST model has been widely employed in the aeroheating predictions for the Mars entry capsules, and shows good agreement with the experimental tests and the predictions of other turbulence models [9, 28]. The non-dimensional turbulent kinetic energy  $k$  and the specific dissipation rate of turbulence  $\omega$  are given by [26]

$$\begin{aligned}\frac{\partial \rho k}{\partial t} + \frac{\partial \rho u_j k}{\partial x_j} &= P_k \left( \frac{Ma}{Re} \right) - \rho \beta^* k \omega + \frac{\partial}{\partial x_j} \left[ \left( \mu + \frac{\mu_T}{\sigma_k} \right) \frac{\partial k}{\partial x_j} \right] \left( \frac{Ma}{Re} \right) \\ \frac{\partial \rho \omega}{\partial t} + \frac{\partial \rho u_j \omega}{\partial x_j} &= P_\omega \left( \frac{Ma}{Re} \right) - \rho \beta \omega^2 \left( \frac{Re}{Ma} \right) + \frac{\partial}{\partial x_j} \left[ \left( \mu + \frac{\mu_T}{\sigma_\omega} \right) \frac{\partial \omega}{\partial x_j} \right] \left( \frac{Ma}{Re} \right) \\ &\quad + 2(1-F_1) \frac{1}{\sigma_\omega} \frac{1}{\omega} \frac{\partial k}{\partial x_j} \frac{\partial \omega}{\partial x_j} \left( \frac{Ma}{Re} \right)\end{aligned}\quad (7)$$

The production source terms are given by [26]

$$P_k = \mu_T \Omega^2, P_\omega = \gamma \rho \Omega^2 \quad (8)$$

where  $\Omega$  is the magnitude of vorticity. The eddy viscosity is given by [26]

$$\mu_T = \min \left[ \frac{\rho k}{\omega}, \frac{a_1 \rho k}{\Omega F_2} \left( \frac{Re}{Ma} \right) \right] \quad (9)$$

There are two sets of constants in the SST model, and the constants used in equations above are blended via [26]

$$\psi = F_1 \psi_1 + (1-F_1) \psi_2 \quad (10)$$

and

$$\begin{aligned}F_1 &= \tanh(\Gamma^4) \\ \Gamma &= \min[\max(\Gamma_1, \Gamma_3), \Gamma_2] \\ \Gamma_1 &= \frac{500\nu}{d^2 \omega} \left( \frac{Ma}{Re} \right)^2, \Gamma_2 = \frac{4\rho k}{d^2 \sigma_{\omega_2} (CD_{k-\omega})}, \Gamma_3 = \frac{\sqrt{k}}{0.09\omega d} \left( \frac{Ma}{Re} \right) \\ CD_{k-\omega} &= \max \left( \rho \frac{2}{\sigma_{\omega_2} \omega} \frac{\partial k}{\partial x_j} \frac{\partial \omega}{\partial x_j}, 1 \times 10^{-20} \right)\end{aligned}\quad (11)$$

where  $d$  is the distance to the nearest wall. The  $F_2$  term is given by [26]

$$\begin{aligned}F_2 &= \tanh(\Pi^2) \\ \Pi &= \max(2\Gamma_3, \Gamma_1)\end{aligned}\quad (12)$$

The constants for set 1 and set 2 are defined as [26]

$$\begin{aligned}\sigma_{k_1} &= 1/0.85, \sigma_{\omega_1} = 1/0.5, \beta_1 = 0.075, \gamma_1 \approx 0.55317 \\ \sigma_{k_2} &= 1.0, \sigma_{\omega_2} = 1/0.856, \beta_2 = 0.0828, \gamma_2 \approx 0.44035\end{aligned}\quad (13)$$

The total viscosity, thermal conductivity and diffusion coefficient are given by [3]

$$\begin{aligned}\mu &= \mu_L + \mu_T \\ \kappa &= \kappa_L + Cp \frac{\mu_T}{Pr_t} \\ D_s &= \left(1 + \frac{\mu_T}{\mu_L} \frac{Sc}{Sc_t}\right) D_{L,s}\end{aligned}\quad (14)$$

where  $\mu$  is total viscosity,  $\mu_L$  is laminar viscosity, and  $\mu_T$  is turbulent viscosity.  $\kappa$  is total thermal conductivity,  $\kappa_L$  is laminar thermal conductivity,  $D_s$  is total diffusion coefficient of species  $s$ , and  $D_{L,s}$  is laminar diffusion coefficient of species  $s$ .  $Cp$  is specific heat at constant pressure,  $Pr$  is laminar Prandtl number,  $Pr_t$  is turbulent Prandtl number,  $Sc$  is laminar Schmidt number, and  $Sc_t$  is turbulent Schmidt number.

The laminar viscosity, thermal conductivity and diffusion coefficient are calculated by collision integrals [3, 23]. The turbulent viscosity is calculated by SST turbulence model, and a nominal value of 0.7 for turbulent Schmidt number is employed [1, 3].

### 2.3 Discretization and boundary conditions

Finite volume method based on multi-block structured meshes is used to solve the governing equations discussed above. The inviscid fluxes are computed using Roe upwind scheme with second order MUSCL reconstruction and minmod limiter [26]. The viscous fluxes are calculated by second order central difference scheme [26]. The implicit Lower-Upper Symmetric Gauss-Seidel (LU-SGS) scheme is employed for time integration.

The recombination processes of atoms release quantities of heat at the surface, and the catalytic properties of the walls can have significant effects on the aeroheating predictions for hypersonic entry capsules [29]. For these complex gas–solid problems, Kovalev and Yakunchikov systematically investigated the gas molecule adsorption and its scattering from the surface through molecular dynamics simulation [30, 31]. These detailed analyses further reveal the mechanism of catalytic properties and provide a reference for more precise aeroheating predictions. However, due to the lack of reliable data, the adsorption characteristics of  $\text{CO}_2$  and  $\text{N}_2$  molecules into PICA (TPS material for the MSL heatshield [14]) in extreme conditions are not clearly known [32]. Thus, supercatalytic boundary condition, which produces the highest possible surface heating prediction and is conservative for the TPS design [32], has been commonly utilized for Mars atmospheric entry simulations for the sake of safety [9, 14, 28]. Given these analyses, supercatalytic boundary condition is employed in the current study to describe the wall catalytic characteristics.

For the solid surface, non-slip wall boundary condition with zero gradient of pressure is implemented. The thermal state of the surface is radiative equilibrium to satisfy the relation  $q_w = \epsilon \sigma T_w^4$ , with a fixed surface emissivity ( $\epsilon$ ) of 0.89 [8, 9, 14]. This model gives the approximate temperature value at each point on the surface and has been extensively utilized for real flight simulations [8, 9, 14]. The chemical composition on the solid surface is supercatalytic to chemical reactions. It is implemented to recombine the species mass fraction to the freestream's value, that is, 97% for  $\text{CO}_2$ , 3% for  $\text{N}_2$ , and zero for other species at the surface in the current simulations. This leads to the maximum surface chemistry contribution to heating and results in conservative heating predictions [3, 28, 32]. It is noted that radiative-equilibrium condition ignores the heat conduction through the TPS material, and supercatalytic wall forces all atoms to recombine to the freestream's value. Both wall conditions are idealized and further researches are still needed to obtain more accurate aeroheating predictions to reduce the TPS requirements in the future.

The symmetry boundary conditions are employed for the symmetry plane. The velocity normal to the symmetry plane is zero, and the normal gradients of all scalar quantities (including species mass fractions) across the symmetry plane are also zero [33, 34].

In addition, the Mach number, static pressure, static temperature and species mass fractions are specified equal to those of the freestream's value for the inlet boundaries, whereas those for the outlet boundaries are obtained through interpolation from the interior of the domain.

## 2.4 Chemical kinetic model

The source terms generally contain two parts, the species source terms  $\omega_s$  and the vibrational energy source term  $\omega_v$ . As mentioned above, the level of thermal non-equilibrium in the flowfield is minor due to short relaxation time of dominant species in the Martian atmosphere  $\text{CO}_2$  [1, 3]. Thus, one temperature model is employed and the vibrational-electronic energy conservation is not included in the current study. The calculations of the species source terms  $\omega_s$  are described as follows.

A chemical kinetic model of Martian atmosphere, including eight species ( $\text{CO}_2$ ,  $\text{CO}$ ,  $\text{N}_2$ ,  $\text{O}_2$ ,  $\text{NO}$ ,  $\text{C}$ ,  $\text{N}$ ,  $\text{O}$ ) and fourteen chemical reactions [35], is implemented in the current study. The mass rate of production of species  $s$  per unit volume is calculated by [23, 24]

$$\omega_s = M_s \sum_{r=1}^{nr} (\beta_{rs} - \alpha_{rs}) [k_{f,r} \prod_{s=1}^{ns} \left(\frac{\rho_s}{M_s}\right)^{\alpha_{rs}} - k_{b,r} \prod_{s=1}^{ms} \left(\frac{\rho_s}{M_s}\right)^{\beta_{rs}}] \quad (15)$$

where  $nr$  is the number of chemical reactions,  $\alpha_{rs}$  and  $\beta_{rs}$  are the stoichiometric coefficients for reactants and products in the  $r$  reaction respectively, and  $k_{f,r}, k_{b,r}$  represent the forward rate coefficient and backward rate coefficient for the  $r$  reaction respectively.

The forward rate coefficients are calculated by Arrhenius expressions, while the backward rate coefficients are obtained via equilibrium constants [23, 24]. The detailed forward and backward rate coefficients of the chemical reactions are calculated by [23, 24]

$$k_{f,r} = C_{f,r} T_d^{n_{f,r}} \exp\left(-\frac{E_{f,r}}{T_d}\right) \quad (16)$$

$$k_{b,r} = \frac{k_{f,r}}{K_{eq}(T_d)} \quad (17)$$

where  $C_{f,r}, n_{f,r}, E_{f,r}$  are the reaction parameters respectively.  $T_d$  is the control temperature of chemical reaction and equals to translational-rotational temperature under the assumption of one temperature model.  $K_{eq}$  represents the equilibrium constant and is evaluated by curve fit [35].

## 3. Computational details

### 3.1. Physical model

In this paper, heatshield configuration based on the MSL capsule is considered. Fig. 1 illustrates the geometries of the heatshield configurations. The diameter of the heatshield is 4.5m, and the radius of nose and shoulder is 1.125m and 0.125m respectively [9]. Three sphere-cone angles, i.e.,  $60^\circ$ ,  $70^\circ$  and  $80^\circ$ , are selected to investigate their effects on the flowfield and the resulting aerothermal characteristics.

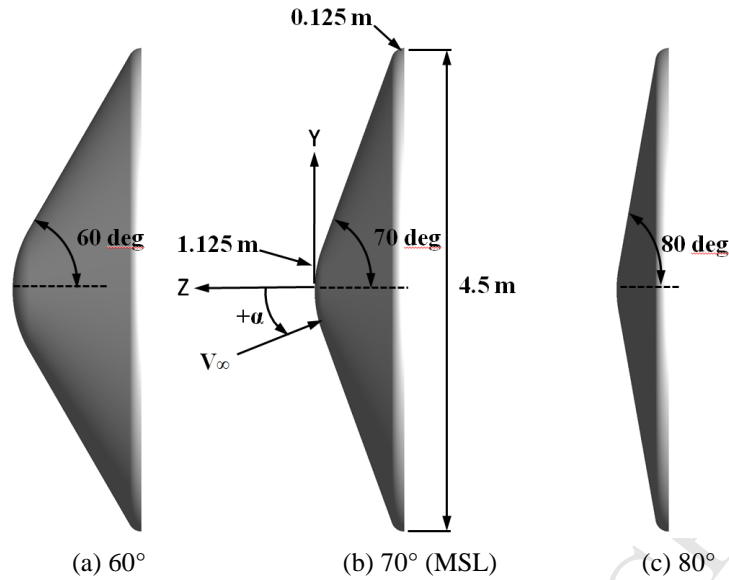


Fig. 1 Heatshield configurations with different sphere-cone angles.

### 3.2. Freestream conditions

A series of flight conditions on  $+3\sigma$  heat load trajectory is run in this study [9]. Detailed freestream parameters are listed in Table 1. Here,  $Re_D$  represents the freestream Reynolds number based on the heatshield's diameter. Previous study [9] has found that peak heat flux is obtained at  $t=71.5$ s along this trajectory. Thus, main attention will be focused on this time point due to its much severer aerothermodynamic environment.

Table 1 Freestream parameters along  $+3\sigma$  heat load trajectory [9].

t(s)	h(km)	$V_\infty$ (km/s)	$\rho_\infty$ (kg/m <sup>3</sup> )	$T_\infty$ (K)	Mach	$Re_D \times 10^{-6}$	$\alpha$ (deg)
64.4	39.7	5.69	$3.51 \times 10^{-4}$	158	28.7	1.14	17.3
69.6	34.0	5.40	$6.63 \times 10^{-4}$	172	26.8	1.87	17.2
71.5	32.2	5.26	$8.22 \times 10^{-4}$	177	26.1	2.19	17.1
76.2	28.0	4.83	$1.18 \times 10^{-3}$	185	23.0	2.74	17.0
84.4	22.4	3.96	$1.96 \times 10^{-3}$	195	18.4	3.52	17.3
100.5	17.1	2.51	$2.86 \times 10^{-3}$	204	11.0	3.11	18.2

### 3.3. Grid generation and sensitivity analysis

Three-dimensional structured meshes with two blocks are constructed for the heatshields. Only half-geometry meshes are generated in this study since sideslip angle is equal to zero. The grid topology and meshes of solid wall, symmetry plane and farfield are displayed in Fig. 2, with elaborate refinement performed at the shock layer and capsule shoulder. Besides, in order to obtain accurate and reliable heating predictions, the cell Reynolds number  $Re_c$  is strictly fixed to be 10 as suggested by Ref. [3, 33]. The cell Reynolds number  $Re_c$ , which governs the first grid spacing at solid wall, is defined as [3, 33]

$$Re_c = \frac{\rho_\infty u_\infty \Delta x_n}{\mu_\infty} \quad (18)$$

where  $\Delta x_n$  is the first normal grid distance close to the wall, and  $\rho_\infty$ ,  $u_\infty$  and  $\mu_\infty$  are freestream density, velocity and viscosity respectively.

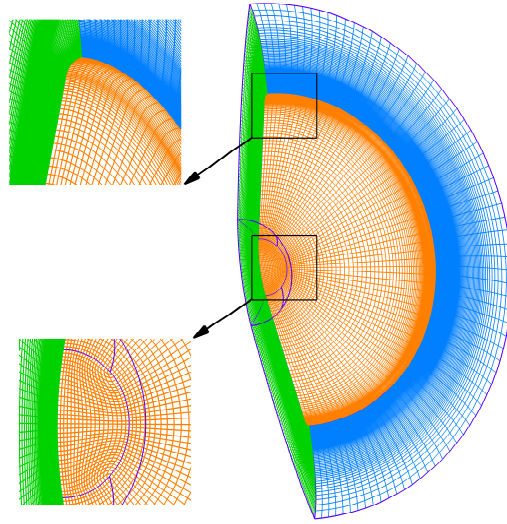


Fig. 2 Meshes for the heatshield (70° sphere-cone case).

To verify the independence of grid resolution, three different grid scales (i.e., coarse, medium, and fine, see Table 2) are compared and analyzed in detail. Laminar and turbulent predictions are conducted on the 70° sphere-cone configuration. Fig. 3 shows the surface heat flux computed by the three grids. It is obvious that the medium and fine grids yield remarkably similar heat flux distributions along the centerline for both laminar and turbulent predictions. Numerical results indicate that the calculations are grid-independent, and thus the medium grid is employed for all cases to achieve a balance between the numerical precision and the computational costs.

Table 2 Grid resolutions.

Grid scale	Grid resolution ( radial $\times$ circumferential $\times$ azimuthal )		Total number of cells
	Block 1	Block 2	
Coarse	93 $\times$ 15 $\times$ 29	93 $\times$ 57 $\times$ 53	303,968
Medium	111 $\times$ 19 $\times$ 37	111 $\times$ 73 $\times$ 69	609,840
Fine	135 $\times$ 27 $\times$ 51	135 $\times$ 105 $\times$ 87	1,372,696

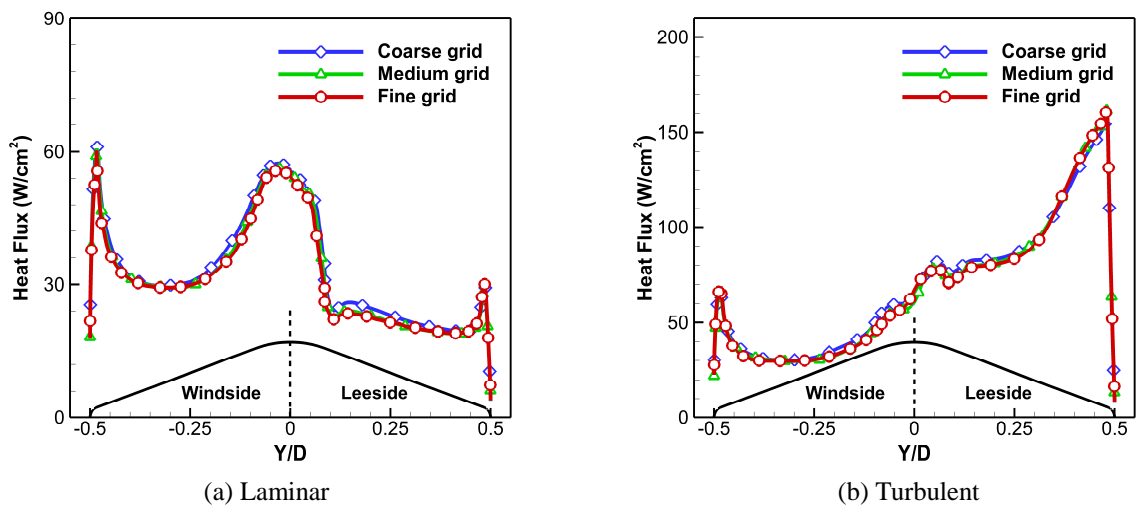


Fig. 3 Surface heat flux comparisons of three grid scales (70° sphere-cone case,  $t=71.5s$ ).

### 3.4. Accumulation of error

Since the governing equations are discretized and solved on finite grid size, a definite error occurs in integration at each step and the accumulation of error is proportional to the number of integration steps [36, 37]. The integration steps in the current study should not exceed the maximal allowable steps that accumulation error exceeds the acceptable value. The maximal allowable number of integration steps is determined by [36, 37]

$$n_{\max} = (S^{\max} / S_{err})^2 \quad (19)$$

where  $S^{\max}$  is total error and presumed to be between 1% and 5%.  $S_{err} \approx \sum_{i=1}^3 S_i$  and  $S_i$  is the relative error of integration in one dimensional case and defined as follow [36, 37]

$$S_i \approx (\Delta L / L_i)^{k+1} \quad (20)$$

where  $\Delta L$  is the mean cell size and  $L_i$  is the domain size in the “ $i$ ” direction,  $k$  is the order of accuracy of numerical scheme.

The ratio of maximal allowable number of integration steps and actual number of steps are defined as follows, the ratio tends to unit when the accumulation error tending to the maximal allowable value [36, 37].

$$R_s = n_{\max} / n \quad (21)$$

In the current study, two blocks of structured meshes are generated for the heatshield configuration and corresponding aerothermodynamics are converged by nearly 50,000 steps. The accumulation error of each block for the three grid scales are arranged in Table 3. As can be seen, all the ratios for the medium grid utilized in this study are larger than unit, which indicates that the accumulation error is not beyond the maximal allowable value.

Table 3 Accumulate error for the three grid scales.

	$S_1$	$S_2$	$S_3$	$S_{err}$	$S^{\max}$	$n$	$n_{\max}$	$R_s$
Coarse grid	1.24E-06	2.96E-04	4.10E-05	3.39E-04	0.05	50,000	2.18E+04	0.44
	1.24E-06	5.40E-06	6.72E-06	1.34E-05	0.05	50,000	1.40E+07	280.13
Medium grid	7.31E-07	1.46E-04	1.97E-05	1.66E-04	0.05	50,000	9.04E+04	1.81
	7.31E-07	2.57E-06	3.04E-06	6.35E-06	0.05	50,000	6.21E+07	1241.63
Fine grid	4.06E-07	5.08E-05	7.54E-06	5.88E-05	0.05	50,000	7.24E+05	14.49
	4.06E-07	8.64E-07	1.52E-06	2.79E-06	0.05	50,000	3.21E+08	6428.53

## 4. Results and discussion

### 4.1. Hypersonic flowfield

Clear comprehension on the hypersonic flowfield is essential to understand the surface conditions and the resulting aerothermal characteristics. The flow structures around the heatshields at the peak heat flux time ( $t=71.5s$ ) are illustrated in Fig. 4. The symmetry plane is colored by Mach number, whereas the heatshield surface is colored by non-dimensional pressure. The stagnation points and streamlines in the symmetry plane and surface are presented as well.

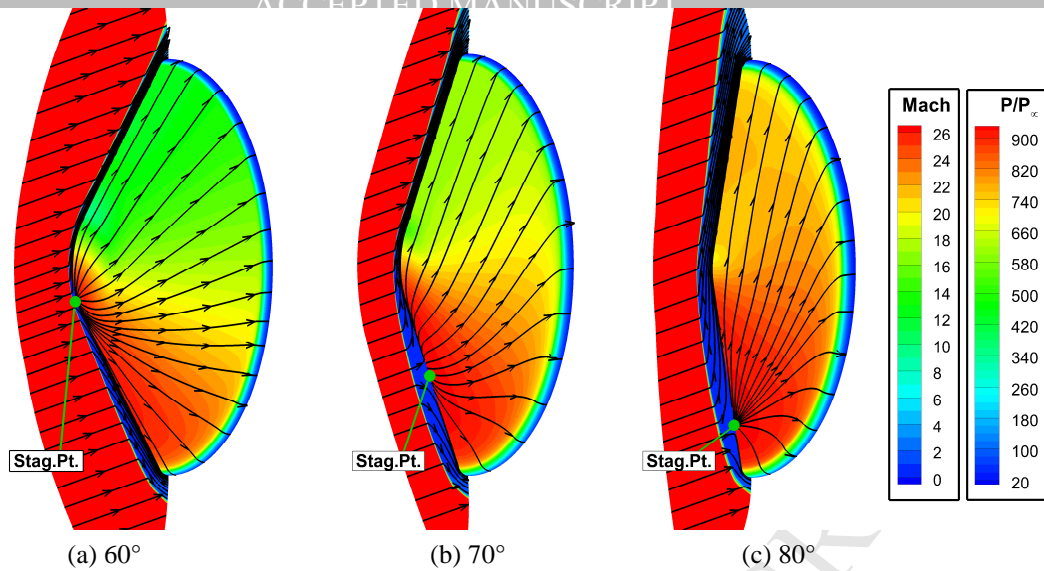


Fig. 4 Symmetry plane cuts of Mach number and surface pressure distributions ( $t=71.5s$ ).

As shown in Fig. 4, a bow shock wave is generated near the heatshield due to the strong compressible effect of the hypersonic flow. The stagnation point moves gradually from the nose to the windside shoulder with the increase of sphere-cone angle. At the windside of heatshield, the shock standoff distances for the 70° and 80° sphere-cone cases are similar, and slightly larger than that for the 60° sphere-cone case. Due to the angle of attack of 17.1°, the freestream is almost perpendicular to the windside of 70° and 80° sphere cone. Therefore, compared to 60° sphere-cone case, the shock waves in the windside for 70° and 80° sphere cones are more like normal shock wave with larger shock standoff distances. At the leeside of heatshield, it is observed that the shock standoff distance gets larger with the increase of sphere-cone angle. These features are confirmed by the distributions of non-dimensional surface pressure. As displayed in Fig. 5, the pressures on the windside surface are almost consistent. Small discrepancy of the location of peak surface pressure occurs due to the shift of stagnation point. At the leeside of heatshield, the surface pressure increases with the increase of sphere-cone angle due to the combination of stronger bow shock wave and weaker flow expansion downstream the nose of heatshield. In addition, it is also observed in Fig. 5 that pressure distributions predicted by laminar and turbulent are nearly identical on the whole surface.

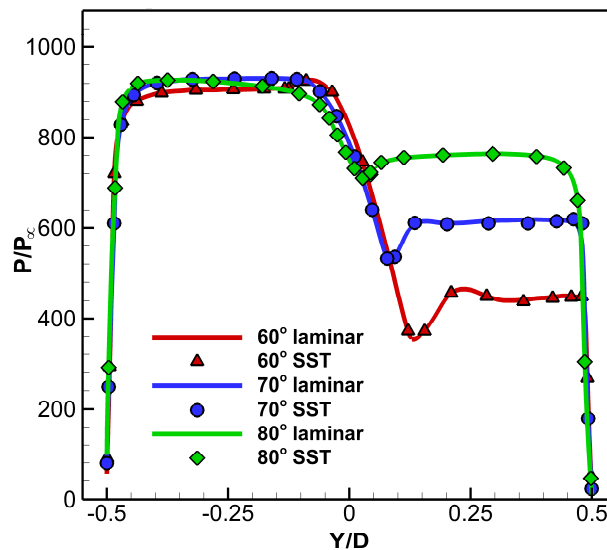


Fig. 5 Comparison of surface pressure on the centerline ( $t=71.5s$ ).

## 4.2 Laminar and turbulent heat flux

The laminar and turbulent heat flux acting on  $60^\circ$ ,  $70^\circ$  and  $80^\circ$  sphere-cone heatshields are presented in Fig. 6. The left half of the figures represents laminar results, whereas the right half represents the turbulent results. As can be seen, the distribution features of laminar heat flux for different configurations are similar. High heat flux is observed at the nose and windside shoulder where the curvature is large. The heat flux is relatively low at the leeside due to the flow expansion downstream the nose. As for turbulent cases, the value of heat flux near the stagnation point is similar to the corresponding laminar results, indicating that the transition has not occurred yet. The flow travels along the surface, and eventually, the laminar boundary layer transits to turbulent one at the leeside of heatshield for all cases. The transition leads to remarkable increase on the heating rates, especially at the leeside shoulder. Besides, much higher turbulent heat flux is observed at the windside of the  $60^\circ$  sphere-cone compared to the laminar prediction. The transition is possible at this area due to the long distance from the stagnation point to the windside shoulder of the sphere-cone. For the remaining areas without flow transition, such as the stagnation point and the nose of heatshield, turbulent heating predictions obtain similar results with the corresponding laminar calculations. Rumsey et al. [38] points out that, SST turbulence model may exhibit certain transition behaviors for fully turbulent external flow computations. Because of no precise transition physics built into the model, the laminar flow region predicted by the turbulence model upstream of transition may be *pseudo-laminar* [38], that is, the predicted laminar region may be numerical. Nevertheless, SST turbulence model can still provide a reference for the flow transition predictions.

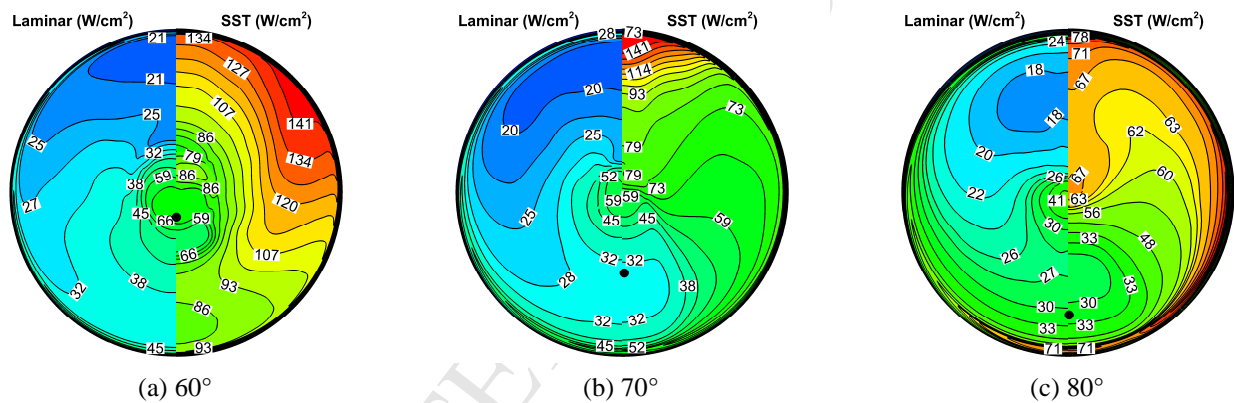


Fig. 6 Laminar and turbulent heat flux (black solid dot represents the stagnation point,  $t=71.5s$ ).

In order to analyze surface aeroheating quantitatively, the laminar and turbulent heat flux on the centerlines are presented and compared in Fig. 7. For laminar predictions shown in Fig. 7 (a), similar heat flux distributions can be observed for the three sphere-cone cases, and smaller sphere-cone angle results in the higher heat flux at the nose. Specifically, the heat flux of the  $60^\circ$  sphere-cone case is higher than the  $70^\circ$  and  $80^\circ$  sphere-cone cases by a factor of about 35% and 70%, respectively. Opposite trend occurs at the windside shoulder, that is, higher heat flux is achieved with the larger sphere-cone angle. This behavior could be ascribed to the curvature change near the shoulder. Besides, at the leeside of heatshield, heat flux is relatively low and insensitive to the sphere-cone angle for most regions. Fig. 7 (b) presents the comparisons of turbulent heat flux on the centerlines. Great discrepancies can be noticed for the three sphere-cone cases. The turbulent heat flux is extremely high at the leeside shoulder for the  $60^\circ$  and  $70^\circ$  sphere-cone cases, and reaches up to  $135W/cm^2$  and  $162W/cm^2$  respectively. However, heat flux at the leeside shoulder is merely about  $81W/cm^2$  for the  $80^\circ$  sphere-cone case. The turbulent heating levels of the  $70^\circ$  and  $80^\circ$  sphere-cones are quite similar in most regions of the windside, i.e., about half of those for the  $60^\circ$  sphere-cone case.

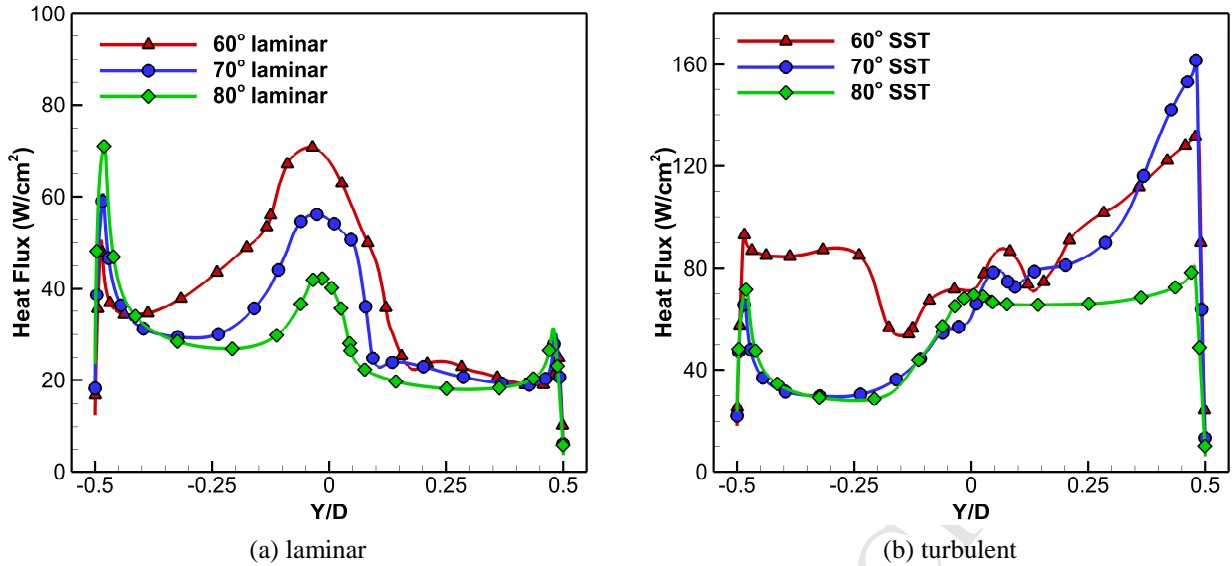


Fig. 7 Comparison of surface heat flux on the centerline ( $t=71.5s$ ).

#### 4.3 Turbulent heating augmentation and transition onset correlations

For configuration analysis and design, it is meaningful to have engineering-level approximation for the transition onset and the resulting turbulent heating augmentation above laminar levels [9, 12]. The turbulent heating augmentation factor  $\phi$  is defined as [3]

$$\phi = \frac{q_{turbulent}}{q_{laminar}} \quad (22)$$

where  $q_{turbulent}$  and  $q_{laminar}$  are the turbulent heat flux and laminar heat flux, respectively.

In the establishment of transition and heating correlations, the laminar boundary-layer momentum thickness Reynolds number  $Re_\theta$  is widely employed [9, 12, 14].  $Re_\theta$  is defined as [14]

$$Re_\theta = \frac{\rho_e u_e \theta}{\mu_e} \quad (23)$$

where  $\rho_e, u_e, \mu_e$  are the density, velocity and viscosity at the boundary-layer edge, respectively. Momentum thickness  $\theta$  is defined as [14]

$$\theta = \int_0^c \frac{\rho u}{\rho_e u_e} \left(1 - \frac{u}{u_e}\right) d\eta \quad (24)$$

It is noteworthy that the boundary-layer edge is defined as the position where the total enthalpy is 99.5% of the freestream value [9, 14].

Previous experimental study provides a correlation between  $\phi$  and  $Re_\theta$ , which is given by

$$\phi = Re_\theta / 158 + 1 \quad (25)$$

The experiment was conducted on a scaled  $70^\circ$  sphere-cone model. The turbulent heat flux was obtained from the wind-tunnel tests, whereas the laminar heat flux and momentum thickness Reynolds number were achieved by the LAURA-based laminar results. Clearly, this linear correlation is very simple to utilize. However, it is hard to fit well the turbulent heating augmentation in the whole  $Re_\theta$  range. Furthermore, the effects of sphere-cone angle are not involved in this correlation.

In this section, a novel correlation for turbulent heating augmentation in terms of laminar momentum thickness Reynolds number, with consideration of sphere-cone angle effect, is developed. The details of the correlation are described as follows.

The correlations of  $\phi$  in terms of  $Re_\theta$  are shown in Fig. 8. The small red symbols represent the current predicted

results of all surface grids on the heatshield. In the process of fitting these points, it is observed that  $\phi$  is approximately linear with the square of  $Re_\theta$ . Besides,  $\phi$  decreases with the increase of sphere-cone angle when  $Re_\theta$  is fixed. Through these relations and a trial-and-error process, we conclude that the turbulent heating augmentation could be correlated by

$$\phi = \frac{\beta}{\alpha_c} \left( \frac{Re_\theta}{1000} \right)^2 + 1 \quad (26)$$

where  $\alpha_c$  is the sphere-cone angle in radians, i.e.,  $6\pi/18$ ,  $7\pi/18$  and  $8\pi/18$  for  $60^\circ$ ,  $70^\circ$  and  $80^\circ$  sphere-cone, respectively.  $\beta$  denotes a constant determined by the freestream conditions.

The developed correlations for different sphere-cone cases are illustrated in Fig. 8. The previous correlation based on the scaled  $70^\circ$  sphere-cone model is also provided as a reference. As can be seen, for different sphere-cone cases, the developed correlations with identical  $\beta=35.6$  can fit well with the current numerical predictions. Our results also demonstrate the obvious differences between correlations based on wind-tunnel tests and real flight conditions. Besides, it is seen that the maximum value of  $Re_\theta$  decreases slightly with the increase of sphere-cone angle. In general, the  $80^\circ$  sphere-cone encounters the least severe turbulent aeroheating environment for a fixed laminar momentum thickness Reynolds number. Transition onset (where  $\phi > 1$  [14]) for all cases occurs when  $Re_\theta \approx 120$ , lower than the corresponding experiment value of about 200 [14]. The numerical results indicate that the transition onset is prematurely predicted. This phenomenon was also observed in previous study [3], and the authors attributed it to the inefficiency of SST turbulence model in predicting the exact location of transition [3].

In order to validate the correlation given by Eq. (23), further investigations are performed at the peak dynamic pressure time ( $t=84.4s$ ). Firstly, the constant  $\beta$  is determined by fitting the predicted  $\phi$  and  $Re_\theta$  results for  $60^\circ$  sphere-cone (Fig. 9 (a)) using Eq. (23). Results indicate  $\beta=21.3$  is appropriate at this freestream condition. Then, by introducing  $\beta=21.3$  into Eq. (23), the correlations for  $70^\circ$  and  $80^\circ$  sphere-cone are also obtained, which are respectively given by

$$\phi = \frac{21.3}{(7\pi/18)} \left( \frac{Re_\theta}{1000} \right)^2 + 1 \quad (27)$$

$$\phi = \frac{21.3}{(8\pi/18)} \left( \frac{Re_\theta}{1000} \right)^2 + 1 \quad (28)$$

Finally, the correlations given by Eq. (24) and (25) are compared with the corresponding predicted results (red symbols) for  $70^\circ$  and  $80^\circ$  sphere-cone cases in Fig. 9 (b) and (c). Similar verification processes are then performed at  $t=76.2s$ , and the corresponding results are displayed in Fig. 10. It is observed that excellent agreements are achieved for different configurations at both time points, indicating satisfactory performances of the correlations in fitting the relationship between  $\phi$  and  $Re_\theta$ . In addition, we can see from Fig. 8-Fig. 10 that with the laminar boundary layer transits to turbulence, the maximum value of  $Re_\theta$  increases obviously from  $t=71.5s$  to  $t=84.4s$ .

The above work shows that the proposed correlation is more accurate and applicable to the aeroheating predictions of heatshields with different sphere-cone angles. Thus, the correlation may provide a means for aerothermodynamics estimation and preliminary design analysis for the future Mars entry capsules.

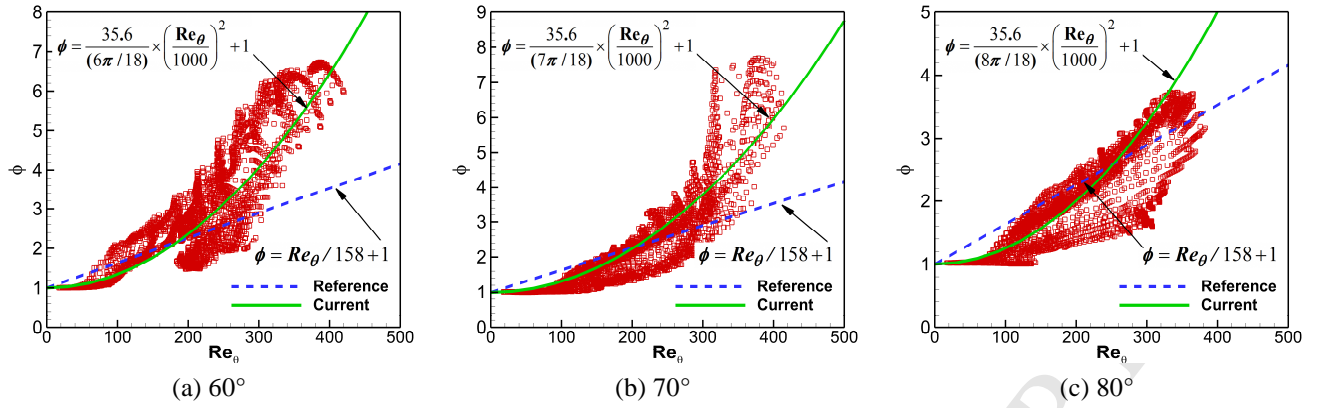


Fig. 8 Correlations of turbulent heating augmentation in terms of momentum thickness Reynolds number ( $t=71.5s$ ).

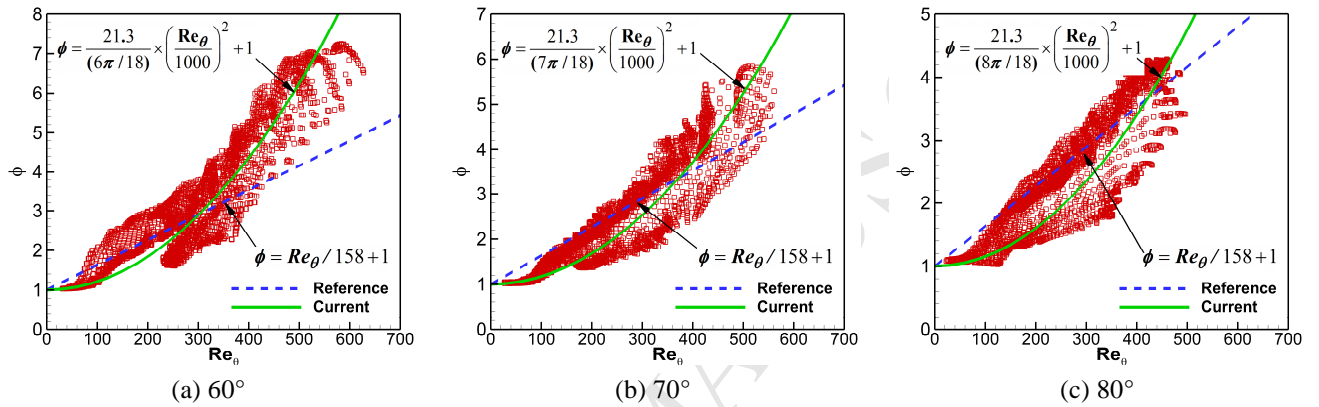


Fig. 9 Correlations of turbulent heating augmentation in terms of momentum thickness Reynolds number ( $t=84.4s$ ).

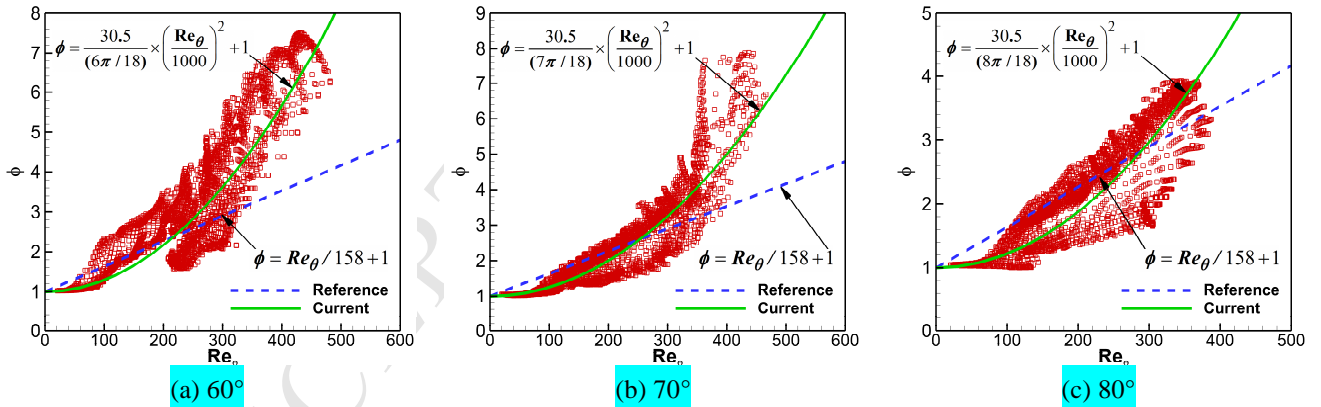


Fig. 10 Correlations of turbulent heating augmentation in terms of momentum thickness Reynolds number ( $t=76.2s$ ).

#### 4.4 Maximum heat flux and total heat load

Maximum heat flux and total heat load are two important components for Thermal Protection System (TPS) design [1]. Maximum heat flux is defined as the maximum value of heat flux found anywhere on the surface of heatshield. This parameter is widely used to determine the TPS material in the design period [1]. Unlike the conventional definition, total heat load herein means the total value of heat flux on the entire surface of heatshield. Similar definition can be found in Ref. [33]. Considering the combination of heating rates and wetting area, this definition is very suitable for evaluation of heatshield configurations in the current study.

The variations of laminar and turbulent maximum heat flux and total heat load for different heatshield configurations along  $+3\sigma$  heat load trajectory are presented in Fig. 11. As can be seen, both the maximum heat flux and total heat load increase to the largest value at the peak heat flux time ( $t=71.5s$ ), and then decrease gradually to a much lower level. Although the trends for different heatshields are similar, obvious discrepancies can be observed in terms of their values. The laminar maximum heat flux for  $60^\circ$  and  $80^\circ$  sphere-cone cases are nearly the same, both higher than the  $70^\circ$  sphere-cone case, with a maximum discrepancy of 20% at  $t=71.5s$ . Quite different scenarios can be found for the turbulent results. The maximum heat flux for the  $80^\circ$  sphere-cone case is remarkably lower than that for the other two cases along the trajectory, especially at the peak heat flux time with about  $80 \text{ W/cm}^2$ , i.e., 100% heat flux reduction observed at this time point.

Comparisons of total heat load for different heatshield configurations are also presented in Fig. 11. The  $80^\circ$  sphere-cone case predicts the lowest total heat load for both laminar and turbulent conditions, and the  $60^\circ$  sphere-cone case achieves the highest one. The discrepancy among these three configurations firstly increases and then decreases along the trajectory. The largest discrepancy occurs at the peak heat flux time. At this time point, the laminar and turbulent total heat load for the  $60^\circ$  sphere-cone case are approximately 32% and 111% higher than those for the  $80^\circ$  sphere-cone case, respectively.

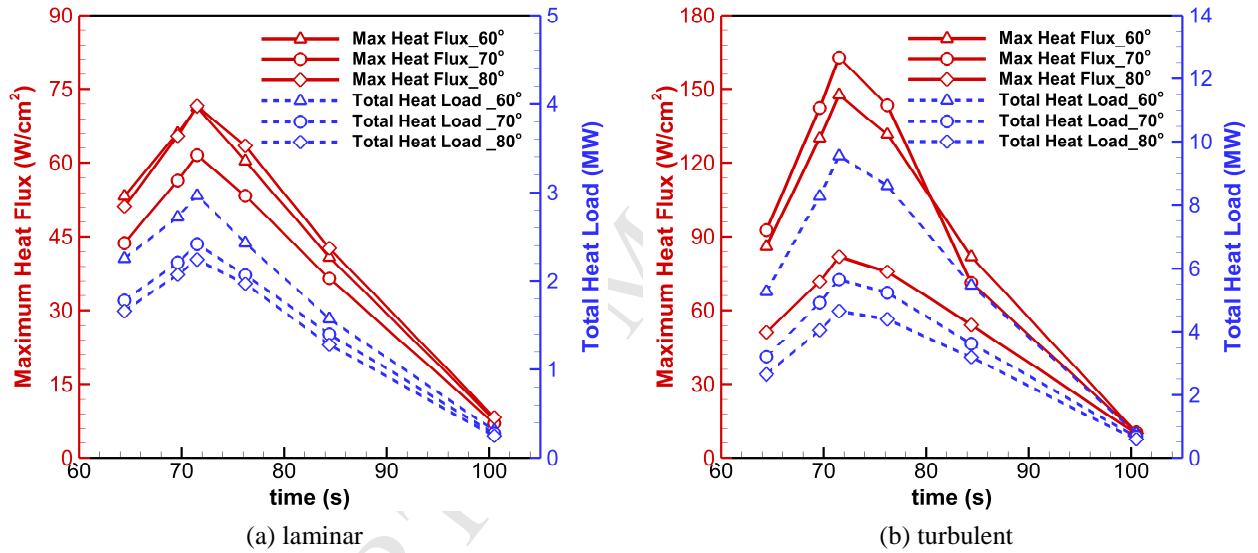


Fig. 11 Maximum heat flux and total heat load along  $+3\sigma$  heat load trajectory.

## 5. Conclusion

This paper conducts a numerical investigation into hypersonic flows over the MSL heatshield with sphere-cone angles of  $60^\circ$ ,  $70^\circ$  and  $80^\circ$ . The flowfield and surface heat flux of different heatshields are examined and compared in detail. A novel correlation for turbulent heating augmentation in terms of laminar momentum thickness Reynolds number is then developed and verified. Finally, the maximum heat flux and total head load along the flight trajectory for different configurations are investigated. Main findings are summarized as follows:

(1). The flow structures of different heatshields are similar except for the shock standoff distance and stagnation point location. The  $80^\circ$  sphere-cone case predicts the largest shock standoff distance, both at the windside and leeside of the heatshield. The stagnation point moves gradually from the nose to the windside shoulder with the increase of sphere-cone angle.

(2). For laminar predictions, larger sphere-cone angle results in lower heat flux at the nose but higher heat flux at the windside shoulder. The heat flux is relatively low and insensitive to the sphere-cone angle at the leeside of heat-

shield. For turbulent predictions, the heating environments for the 60° and 70° sphere-cone cases are significantly severer than the 80° sphere-cone case, especially at the leeside shoulder.

(3). A novel correlation between turbulent heating augmentation and laminar momentum thickness Reynolds number, with consideration of sphere-cone angle effect, is developed. Numerical investigations indicate that the proposed correlation is more accurate and applicable to the aeroheating predictions of heatshields with different sphere-cone angles.

(4). Along the trajectory, both maximum heat flux and total heat load firstly increase to the largest values at the peak heat flux time, and then decrease gradually to a much lower level. The turbulent maximum heat flux of the 80° sphere-cone case is remarkably lower than the other two cases, especially at the peak heat flux time. Besides, the 80° sphere-cone case obtains the lowest total heat load for both laminar and turbulent predictions along the trajectory, and the 60° sphere-cone case predicts the highest values.

Numerical results in this paper demonstrate the significant effects of sphere-cone angle on aerothermodynamics of heatshield configurations for Mars entry capsules, especially at the leeside in turbulent flows. Moreover, compared to the conventional heatshield configuration, the 80° sphere-cone exhibits obvious advantages in the turbulent heating predictions. This is worth noticing in the heatshield design and optimization for future Mars entry capsules.

### Conflict of interest statement

The authors declare that they have no conflict of interests.

### Acknowledgements

This work was supported by grants from the National Natural Science Foundation of China (No. 11721202). The first author, Kang Zhong would also like to express his sincere thanks to Hongkang Liu and Yatian Zhao from Beihang University.

### References:

- [1] M.J. Wright, C.Y. Tang, K.T. Edquist, A Review of Aerothermal Modeling for Mars Entry Missions, AIAA 2010-443, 2010.
- [2] J. Hao, J. Wang, Z. Gao, C. Jiang, C. Lee, Comparison of transport properties models for numerical simulations of Mars entry vehicles, *Acta Astronaut.*, 130 (2017) 24-33.
- [3] X. Wang, C. Yan, W. Zheng, K. Zhong, Y. Geng, Laminar and turbulent heating predictions for mars entry vehicles, *Acta Astronaut.*, 128 (2016) 217-228.
- [4] Bonn B. Kirk, Peter F. Intrieri, Alvin Seiff, Aerodynamic Behavior of the Viking Entry Vehicle: Ground Test and Flight Results, *J. Spacecraft*, 15 (1978) 208-212.
- [5] G. Peter A., B. Robert D., W. K. James, M. Robert A., E. Walter C., P. Richard W., Prediction and Validation of Mars Pathfinder Hypersonic Aerodynamic Data Base, *J. Spacecr. Rocket.*, 36 (1999) 367-373.
- [6] B. Raiszadeh, P. Desai, R. Michelltree, Mars Exploration Rover Heat Shield Recontact Analysis, AIAA 2011-2584, 2011.
- [7] K.T. Edquist, P.N. Desai, M. Schoenenberger, Aerodynamics for Mars Phoenix Entry Capsule, *J. Spacecr. Rocket.*, 48 (2011) 713-726.
- [8] D. Bose, T. White, M. Mahzari, K. Edquist, Reconstruction of Aerothermal Environment and Heat Shield Response of Mars Science Laboratory, *J. Spacecr. Rocket.*, 51 (2014) 1174-1184.
- [9] K.T. Edquist, A.A. Dyakonov, M.J. Wright, et al., Aerothermodynamic Environments Definition for the Mars Science Laboratory Entry Capsule, AIAA 2007-1206, 2007.
- [10] B.R. Hollis, D.S. Liechty, M.J. Wright, M.S. Holden, T.P. Wadhams, M. Maclean, A. Dyakonov, Transition Onset and Turbulent Heating Measurements for the Mars Science Laboratory Entry Vehicle, AIAA 2005-1437, 2005.
- [11] H. Johnson, G. Candler, M. Wright, Boundary Layer Stability Analysis of Mars Science Laboratory Aeroshell, AIAA 2006-920, 2006.
- [12] B. Hollis, Blunt-Body Entry Vehicle Aerothermodynamics: Transition and Turbulence on the CEV and MSL Configurations, *J. Spacecr. Rocket.*, 49 (2012) 435-449.

- [13] M. Wright, J. Olejniczak, J. Brown, H. Hornung, K. Edquist, Computational Modeling of T5 Laminar and Turbulent Heating Data on Blunt Cones, Part 2: Mars Applications, AIAA 2005-177, 2005.
- [14] K.T. Edquist, B.R. Hollis, C.O. Johnston, D. Bose, T.R. White, M. Mahzari, Mars Science Laboratory Heatshield Aerothermodynamics: Design and Reconstruction, *J. Spacecr. Rocket.*, 51 (2014) 1106-1124.
- [15] M.J. Wright, J. Olejniczak, J.L. Brown, H.G. Hornung, K.T. Edquist, Modeling of Shock Tunnel Aeroheating Data on the Mars Science Laboratory Aeroshell, *J. Thermo. Heat Trans.*, 20 (2006) 641-651.
- [16] C.L. Chang, M.M. Choudhari, B.R. Hollis, Transition Analysis for the Mars Science Laboratory Entry Vehicle, AIAA 2009-4076 (2009).
- [17] A.G. Neville, G.V. Candler, Computational-Fluid-Dynamics-Based Axisymmetric Aeroshell Shape Optimization in Hypersonic Entry Conditions, *J. Space. Rocket.*, 52 (2015) 76-88.
- [18] J.L. Brown, The effect of forebody geometry on turbulent heating and thermal protection system sizing for future Mars mission concepts, in: *Proceeding of the 4th International Planetary Probe Workshop*, Pasadena, CA, June 2006.
- [19] S. Ju, C. Yan, X. Wang, Y. Qin, Z. Ye, Sensitivity analysis of geometric parameters upon the aerothermodynamic performances of Mars entry vehicle, *Int. J. Heat Mass Transfer*, 120 (2018) 597-607.
- [20] B.R. Hollis, A.S. Collier, Turbulent Aeroheating Testing of Mars Science Laboratory Entry Vehicle, *J. Space. Rocket.*, 45 (2008) 417-427.
- [21] X. Yang, W. Tang, Y. Gui, Y. Du, G. Xiao, L. Liu, Hypersonic static aerodynamics for Mars science laboratory entry capsule, *Acta Astronaut.*, 103 (2014) 168-175.
- [22] X. Wang, C. Yan, S. Ju, Y. Zheng, J. Yu, Uncertainty analysis of laminar and turbulent aeroheating predictions for Mars entry, *Int. J. Heat Mass Transfer*, 112 (2017) 533-543.
- [23] P.A. Gnoffo, R.N. Gupta, J.L. Shinn, Conservation equations and physical models for hypersonic air flows in thermal and chemical nonequilibrium, NASA TP-2867, 89 (1989).
- [24] G.S.R. Sarma, Physico-chemical modelling in hypersonic flow simulation, *Prog. Aeros. Sci.*, 36 (2000) 281-349.
- [25] F.R. Menter, Two-equation eddy-viscosity turbulence models for engineering applications, *AIAA J.*, 32 (1994) 1598-1605.
- [26] K. Sherrie L., B. Robert T., R. Christopher L., CFL3D User's Manual (Version 5.0), NASA Langley Technical Report Server, 1998.
- [27] J. Brown, Turbulence Model Validation for Hypersonic Flows, AIAA 2002-3308, 2002.
- [28] K. Edquist, A. Dyakonov, M. Wright, C. Tang, Aerothermodynamic Design of the Mars Science Laboratory Heatshield, AIAA 2009-4075, 2009.
- [29] V. Kovalev, V. Sazonenko, A. Yakunchikov, Dynamic Monte Carlo simulation of surface recombination, *Moscow University Mechanics Bulletin*, 62 (2007) 53-58.
- [30] V. Kovalev, A. Yakunchikov, F. Li, Simulation of hydrogen adsorption in carbon nanotube arrays, *Acta Astronaut.*, 68 (2011) 681-685.
- [31] V. Kovalev, A. Yakunchikov, F. Li, Tangential momentum and thermal accommodation coefficients for hydrogen molecules on graphite surface, *Acta Astronaut.*, 69 (2011) 744-746.
- [32] B.R. Hollis, D.K. Prabhu, M. Maclean, A. Dufrene, Blunt-Body Aerothermodynamic Database from High-Enthalpy Carbon-Dioxide Testing in an Expansion Tunnel, *J. Thermo. Heat Trans.*, 31 (2017) 712-731.
- [33] J. Guo, G. Lin, X. Bu, S. Fu, Y. Chao, Effect of static shape deformation on aerodynamics and aerothermodynamics of hypersonic inflatable aerodynamic decelerator, *Acta Astronaut.*, 136 (2017) 421-433.
- [34] W. Liu, L. Zhang, Y. Wang, et al., *Foundations of Computational Aerodynamics Parallel Programming*, National Defense Industry Press, Beijing, 2013 (in Chinese).
- [35] R.A. Mitcheltree, P.A. Gnoffo, Wake flow about a MESUR Mars entry vehicle, AIAA 94-1958 (1994).
- [36] N.N. Smirnov, V.B. Betelin, V.F. Nikitin, et al., Accumulation of errors in numerical simulations of chemically reacting gas dynamics, *Acta Astronaut.*, 117 (2015) 338-355.
- [37] N.N. Smirnov, V.B. Betelin, R.M. Shagaliev, et al., Hydrogen fuel rocket engines simulation using LOGOS code, *Inter. J. Hydrogen Energy*, 39 (2014) 10748-10756.
- [38] C.L. Rumsey, Apparent transition behavior of widely-used turbulence models, *Inter. J. Heat & Fluid Flow*, 28 (2007) 1460-1471.

## Highlights

- Flow over heatshields with 60°, 70° and 80° sphere-cone angles is investigated.
- Laminar and turbulent heat flux are simulated and compared in detail.
- A novel correlation for turbulent heating augmentation in terms of  $Re_\theta$  is developed.
- Maximum heat flux and total heat load along the flight trajectory are investigated.